PHYSICAL REVIEW RESEARCH **6**, L032027 (2024)

Letter

Experimental observation of parabolic wakes in thin plates

Janez Rus,[*] Aleksi Bossart, Benjamin Apffel, Matthieu Malléjac, and Romain Fleury[†]
Laboratory of Wave Engineering, Institute of Electrical and Micro Engineering, Ecole Polytechnique Fédérale de Lausanne (EPFL), Station 11, 1015 Lausanne, Switzerland

(Received 7 February 2024; accepted 3 July 2024; published 2 August 2024)

Wakes are medium perturbations created by a moving object, such as wave patterns behind boats, or wingtip vortices following an aircraft. Here, we report about an experimental study of an uncharted form of parabolic wakes occurring in media with the group velocity twice larger than the phase velocity, as opposed to the conventional case of Kelvin wakes. They are formed by moving a laser spot on a thin plate, which excites a unique wake pattern made of confocal parabolas, due to the quadratic dispersion of the zero-order flexural Lamb mode. If the spatial dimensions are rescaled by the perturbation velocity and material constant, we obtain a single universal wake with constant parabolic focal lengths. We demonstrate an evanescent regime above the critical frequency where the wave components oscillate exclusively in the direction parallel to the perturbation path, with an opening angle of 90°. We define a dimensionless number, analogous to Froude and Mach numbers, which determines whether or not the complete parabolic wake pattern will be excited by the moving source. Finally, we generalize the physics of wake shapes to arbitrary dispersion relations.

DOI: 10.1103/PhysRevResearch.6.L032027

The broadest definition of wakes refers to a pattern, typically made of waves, excited by the movements of an object or a perturbation in a medium. The most prominent example is the Kelvin wake pattern generated by a moving object on the surface of water [1–12]. A second common use of the term wake is associated with the circulating turbulent flow behind a moving object in a fluid (Kármán vortex) [13,14], as seen with phenomena like wingtip vortices behind an aircraft [15–18]. Additional associations encompass wakes formed behind charged objects in supersonic plasma flows [19–21] or laser-driven plasma wake fields [22–25], which show promise as an alternative method for electron acceleration. This definition also includes Mach cones [20,26] or Cherenkov radiation [27–30], which are less often called wakes due to the absence of dispersion wave interference.

The wake pattern on the surface of deep water depends on whether the dispersion is capillary dominated [31–33], with $\omega \propto k^{3/2}$ being the relation between angular frequency ω and wave number k, or if it is gravity dominated [8,34], with $\omega \propto k^{1/2}$. The latter power law yields the commonly observed Kelvin wake pattern, typical of the wakes originating from ducks or boats as they move. The Kelvin wake patterns exhibit the remarkable property that their shape, in the case of sufficiently slow movements, is independent of the perturbation velocity, when properly rescaled coordinates are used. The half-cone opening angle is constant at the value $\arcsin(1/3) \cong 19.47^\circ$. This is a well-researched situation of the wakes on water where the group velocity is twice lower than the phase velocity.

Our motivation is to extend the scope of the wake research to general power laws by proving that the wakes can be observed in media with different dispersion properties and even in solids. In this work, we experimentally explore the behavior of wake patterns excited in a medium in which the power law governing the dispersion relation is exactly inverse to the one of Kelvin wakes, namely $\omega \propto k^2$. These wakes are obtained behind a fast-moving perturbation on a thin plate. The zero-order asymmetric Lamb mode of the plate exhibits a dispersion relation well approximated by $\omega = k^2/\alpha$, where α is a constant dependent on the thin plate thickness and material properties. The group velocity $c_g = d\omega/dk = 2k/\alpha$ is therefore twice higher than the phase velocity $c_{\mathrm{ph}} = \omega/k = k/\alpha$, and proportional to the square root of frequency, setting a unique stage for the study of the new form of wakes.

The perturbation in our case is a focused laser beam illuminating the surface of a polymer plate [Fig. 1(a)]. The induced heating leads to a localized reduction in the Young's modulus of the plate. The flexural Lamb waves are excited due to the temperature gradient and the uneven temperature expansion along the plate thickness at the heated position. In our experiment, galvanometric scanning mirrors were used to displace the heated position at constant velocities v_{p} in a linear trajectory. The angle between the plate surface and the laser beam was set to 20° at the midpoint of the scanning area. Consequently, a small change in the galvanometric mirror's angle provided a large alteration in the perturbation's position. This, in turn, allowed us to achieve perturbation velocities v_{p} fast enough to observe a broad range of parabolic wakes. Moreover, this setup enabled us to investigate the impact of the laser spot size on the formation of the parabolic wakes.

---

[*] Contact author: janez.rus@tum.de
[†] Contact author: romain.fleury@epfl.ch

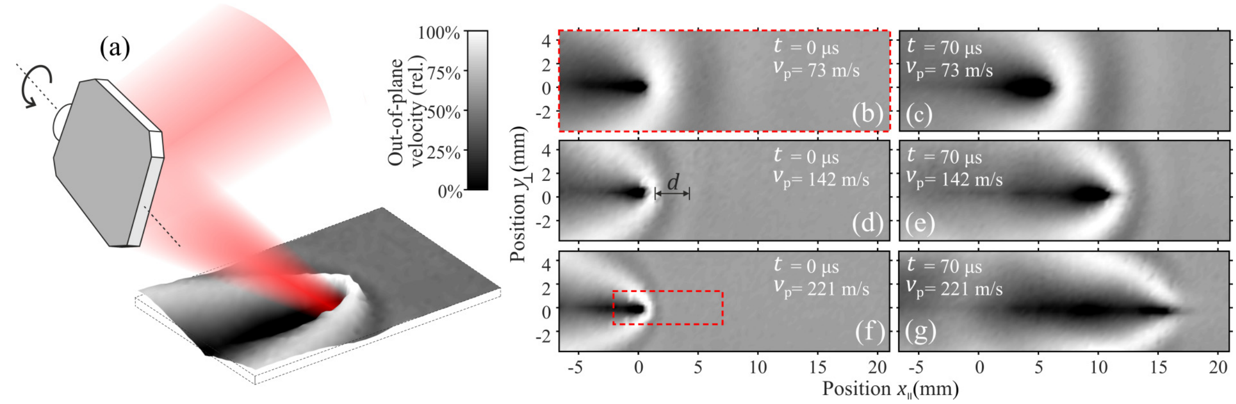

FIG. 1. Schematic of the setup, where a moving laser beam excites elastic waves on a thin plate (a). Measured parabolic wake patterns at $t = 0$ µs (b), (d), (f) and $t = 70$ µs (c), (e), (g) at three distinct perturbation velocities v_p [(b), (c), (d), (e), and (f), (g)]. The red dashed-line square in (f) shows a portion of the wake whose shape is identical to the one observed over the full range in (b), when both axes are rescaled by a factor 3, corresponding to the ratio of v_p values in these two cases.

For more details regarding the experimental procedure and the setup, please refer to the Supplemental Material [35].

In Figs. 1(b)–1(g), we present the parabolic wakes captured by a laser vibrometer for three distinct v_p values and two different time instances. The out-of-plane velocity of the plate was measured for each scanning position through separate wake excitations. The excitation laser was in focus at the position $x_\parallel = 0$, corresponding to time $t = 0$ [Figs. 1(b), 1(d), and 1(f)]. Additional wakes for 12 different v_p values and a scenario involving an elevated temperature of the polymer plate are presented in the Supplemental Material [35].

The wave pattern shape of Fig. 1(b) is identical to that confined within the red dashed-line square in Fig. 1(f), which has both axes reduced by a factor 3, chosen to correspond to the ratio between the values of $v_p = 221$ m/s in Fig. 1(f) and $v_p = 73$ m/s in Fig. 1(b). In contrast, Kelvin wakes follow an inverse rescaling law, where higher v_p provide larger dominant wavelengths, while rescaling of spatial coordinates in both directions does not change the cone opening angle. In our case, the measured parabolas all have a curvature that linearly increases with v_p. The focal distance, which is inversely proportional to the curvature of the parabolic ridges in Figs. 1(b)–1(g), is therefore inversely proportional on v_p.

As wakes result from the interference of many frequency components, we propose to study the different spectral components of the wakes separately. As examples, we show in Figs. 2(d)–2(f) [respectively Figs. 2(g)–2(i)] the measured scans from Figs. 1(b) and 1(c) at $v_p = 73$ m/s [respectively from Figs. 1(f) and 1(g) at $v_p = 221$ m/s], filtered to three selected narrow-band frequencies, which were then processed to obtain data points in Figs. 2(a)–2(c), marked by yellow squares (respectively green circles).

In our experiment [Fig. 2(a)], we observe that the wave number of the wakes in the direction parallel to the motion is fixed by v_p, and follows the law

$$k_\parallel(\omega) = \frac{\omega}{v_p}. \tag{1}$$

In particular, it is neither influenced by the dispersion law of the medium nor the wave velocities in the medium. Instead, its dependency on ω is entirely determined by v_p. This condition matches the parallel projection of the phase velocity with the source velocity. Using the dispersion law $\omega = k^2/\alpha$ where $k = \sqrt{k_\parallel^2 + k_\perp^2}$, we can express the wave number of the wakes in the direction perpendicular to v_p:

$$\begin{aligned} k_\perp(\omega) &= \sqrt{\alpha\omega - k_\parallel^2} \\ &= \sqrt{\alpha\omega - \frac{\omega^2}{{v_p}^2}} = \alpha v_p \sqrt{\frac{\omega}{\alpha {v_p}^2} - \frac{\omega^2}{\alpha^2 {v_p}^4}}. \end{aligned} \tag{2}$$

If we introduce rescaled variables $\hat{k}_\perp = k_\perp/\alpha v_p$ and $\hat{k}_\parallel = k_\parallel/\alpha v_p$, as well as $\hat{\omega} = \omega/\alpha {v_p}^2$, we can simplify Eqs. (1) and (2) to

$$\hat{k}_\parallel(\hat{\omega}) = \hat{\omega}, \quad \hat{k}_\perp(\hat{\omega}) = \sqrt{\hat{\omega} - \hat{\omega}^2}. \tag{3}$$

The above formula for rescaled wave numbers $\hat{k}_\parallel(\hat{\omega})$ and $\hat{k}_\perp(\hat{\omega})$ is represented in Figs. 2(a) and 2(b) with thick red lines and compared to the experimental results obtained for ten different source velocities ranging from 73 m/s to 292 m/s identifiable by the shades of gray. The opening angle between the propagation direction of the wave component and the direction perpendicular to the source motion at a specific frequency, $\varphi(\hat{\omega}) = \arctan\,(\hat{k}_\parallel(\hat{\omega})/\hat{k}_\perp(\hat{\omega}))$, is also shown in Fig. 2(c). As a result of the rescaling, the darker shades of gray, corresponding to higher v_p, stop at lower values of $\hat{\omega}$ in Figs. 2(a)–2(c), even though the range of nonrescaled ω is constant for all v_p. Figures 2(a)–2(c) in their original (nonrescaled) coordinates are provided in the Supplemental Material [35].

Equation (3) predicts that $\hat{k}_\perp(\hat{\omega})$ is real for $\hat{\omega} < 1$, when ω is smaller than the critical frequency $\omega_{cr} = \alpha v_p^2$. The angle $\varphi(\hat{\omega})$ increases until it reaches 90° at ω_{cr}. This is the highest frequency at which the wake components are purely propagating. The wake component at ω_{cr} propagates in the direction parallel to the perturbation path with the velocity equal to v_p. It can therefore be directly expressed as $\omega_{cr} = v_p/d$, where d is the distance between the vertices of two parabolas defined by the maximum ridges of the wake pattern [Fig. 1(d)]. Interestingly, an opposite behavior is true for Kelvin wakes.

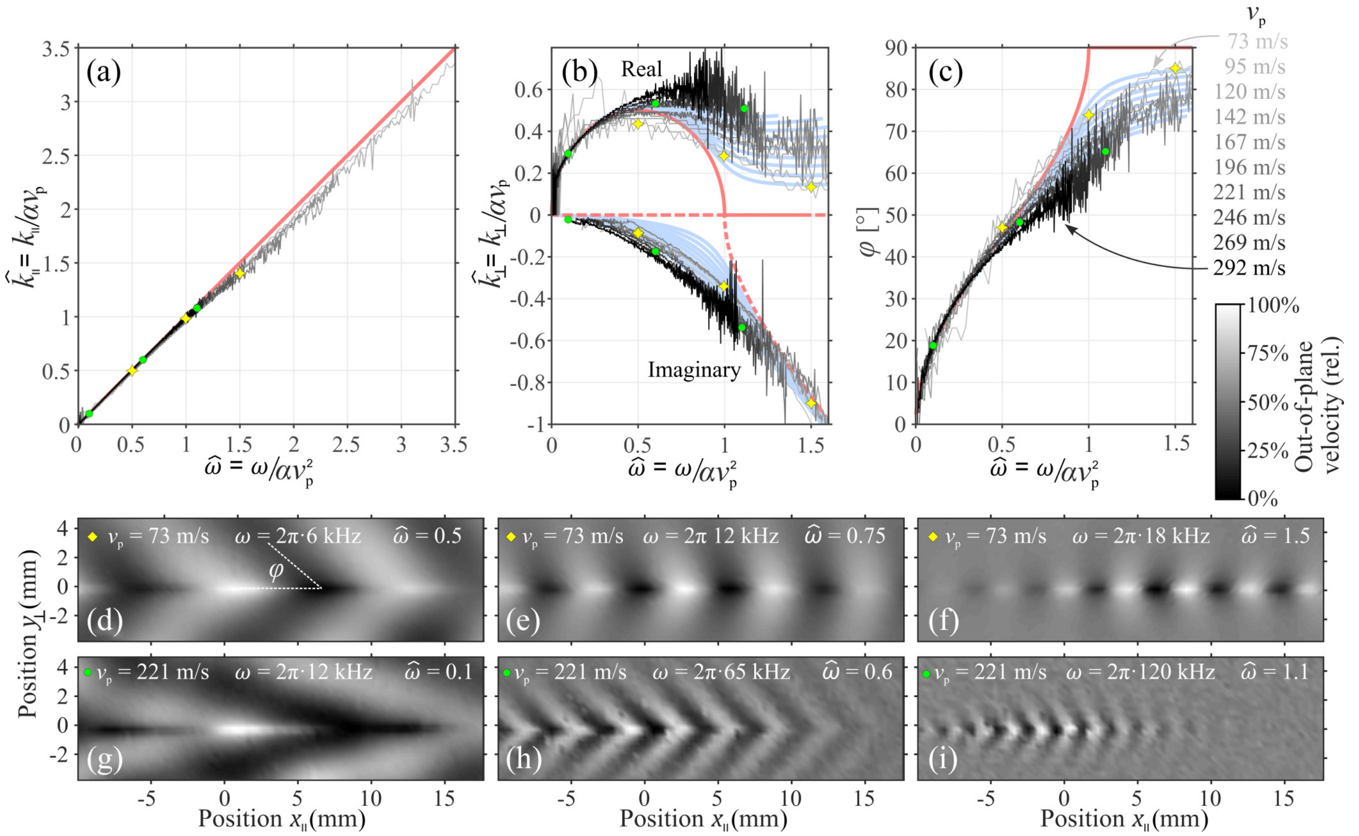

FIG. 2. The measured wave numbers $\hat{k}_\parallel$ (a) and $\hat{k}_\perp$ (b) for ten different v_p values (grey lines) collapse on the red curves predicted by Eq. (3) except near the critical frequency (at $\hat{\omega} = 1$). Around the critical frequency, variations in the perturbation size along the position $x_\parallel$ (due to the laser beam moving in and out of focus) become important. These variations are accounted for in a refined model (blue lines). The angle φ between the direction of v_p and the wave fronts becomes larger as $\hat{\omega}$ increases, reaching almost 90° at the critical frequency $\hat{\omega} = 1$ (c). Beyond this frequency, Eq. (3) predicts that $\hat{k}_\perp$ becomes imaginary, which defines the evanescent regime (f). When the parabolic wake patterns from Fig. 1 are filtered to narrow frequencies (d)–(i), represented by yellow squares and green circles, the openings of the wave fronts adhere to the Mach law in respect to the wave velocity at the specific frequency.

The $k_\perp(\omega)$ of Kelvin wakes is real above a critical frequency, which can be estimated from the wavelength of the wave components propagating directly behind the moving perturbation.

For parabolic wakes, $\hat{k}_\perp(\hat{\omega})$ is imaginary at $\hat{\omega} > 1$. In this evanescent regime, wave components are localized to the vicinity of the perturbation path, oscillating only along the direction parallel to v_p, as governed by Eq. (1). This effect is evident in Fig. 2(f). The exponential decay length in the direction perpendicular to v_p of the evanescent waves decreases with increasing frequencies. Due to the limited frequency range of the measuring system and the increase of intrinsic losses at higher frequencies, the evanescent regime ($\hat{\omega} > 1$) is more easily observed in the measurements performed at lower v_p.

While $\hat{k}_\parallel$ falls on the same curve for all v_p values, there is a greater discrepancy between the measured $\hat{k}_\perp$ and Eq. (3), especially around ω_{cr}. This arises due to variations in laser beam diameter as it moves along in the direction of v_p. As the beam approaches the focal point, higher frequency components are stimulated with higher amplitudes (and conversely as it moves away from the focal point). These alterations of the excitation amplitude spectrum along $x_\parallel$ leads to a nonzero imaginary part of $\hat{k}_\parallel$. As a result, the imaginary part of $\hat{k}_\perp$ becomes nonzero even below the critical frequency, and the real part of $\hat{k}_\perp$ is underestimated by Eq. (2) when nearing ω_{cr} [Fig. 2(b)]. This effect becomes more pronounced for larger v_p values. Consequently, for the field map of Fig. 2(i), the angle φ is 65° [green point in Fig. 2(c)], instead of 90° as predicted by the theory. The effect of the laser focusing and defocusing along the position $x_\parallel$ can be accounted for in a refined model (Supplemental Material [35]), yielding the thick blue lines, which fit the measurements better than the reduced model of Eq. (3).

Having understood how each frequency behaves individually, we can now express the wake pattern as the real part of the following sum over all excited waves that verify Eqs. (1) and (2):

$$\begin{aligned} Z(x,y,t) &= \int_0^{\omega_{\text{Max}}} A(\omega) e^{-ik_x x} e^{-ik_y y} e^{-i\omega t} d\omega \\ &= \int_0^{\omega_{\text{Max}}} A(\omega) e^{-i(\omega/v_p)x} e^{-i\sqrt{\alpha\omega - (\omega^2/v_p{}^2)}\, y} e^{-i\omega t} d\omega. \end{aligned} \tag{4}$$

ω_{Max} represents the highest frequency being excited, while $A(\omega)$ is the excitation amplitude at a given ω. The amplitude spectrum of the measured parabolic wake is provided in the

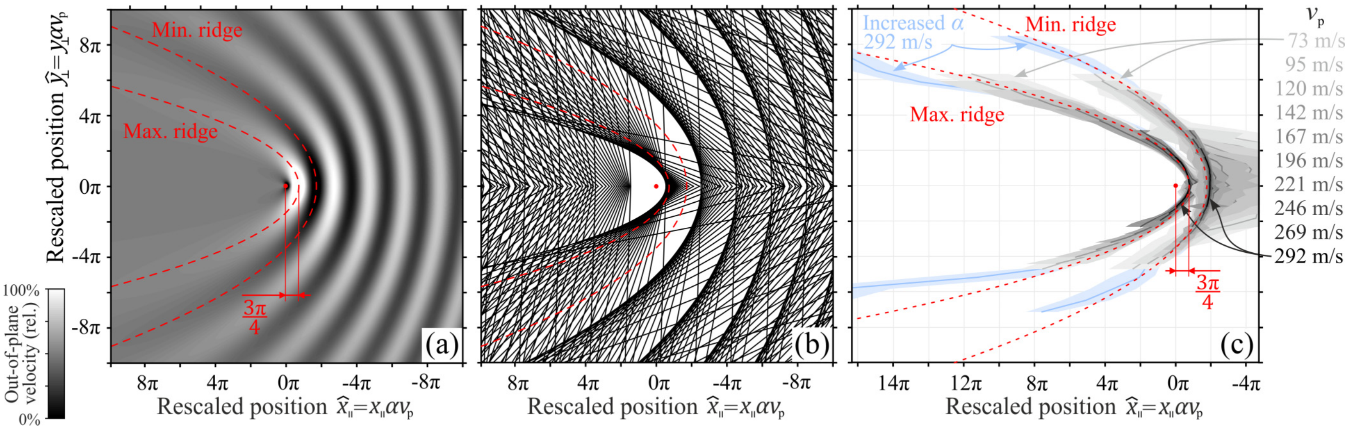

FIG. 3. Time derivative of Eq. (5) obtained by the stationary phase approximation (a). The maximum ridges of the pattern follow shapes of confocal parabolas, having focal lengths $\widehat{f}_n = \phi_p + \pi/4 + 2\pi n$, where $\phi_p = \pi/2$ due to the velocity measurement. The parabolic shape of the interference pattern can be elucidated through the concept of parallel lines (wave fronts) (b). Their slope (or angle φ) is computed from their periodicity (wavelength) using the dispersion relation. Their origin corresponds to the phase of the wake excitation. If the dimensions $x_\parallel$ and $y_\perp$ are rescaled by the factor αv_p, the maximum and minimum ridges observed in the measurement (full wakes at three chosen speeds shown in Fig. 1) align with the two confocal parabolas (red dashed lines) with focal lengths of $3\pi/4$ and $3\pi/4 + \pi$, respectively, across all ten different v_p [(c), gray shades] as well as for the scenario when α is increased [(c), blue].

Supplemental Material [35] for 12 different perturbation velocities v_p.

Using the same rescaled variables as those employed for Eq. (3), the out-of-plane displacement of the interference wake pattern can be formulated in rescaled position coordinates: $\hat{x}_\parallel = x_\parallel \alpha v_p$, $\hat{y}_\perp = y_\perp \alpha v_p$, and rescaled time $\hat{t} = t \alpha {v_p}^2$ as

$$Z(\hat{x}_\parallel, \hat{y}_\perp, \hat{t}) = \int_0^{\hat{\omega}_{\text{Max}}} A(\hat{\omega}) e^{-i\hat{\omega}\hat{x}} e^{-i\sqrt{\hat{\omega} - \hat{\omega}^2}\,\hat{y}} e^{-i\hat{\omega}\hat{t}} d\hat{\omega}. \quad (5)$$

Analogously to the case of Kelvin wakes, the integral solution can be expressed using the stationary phase approximation (please refer to the Supplemental Material [35]). In order to explain the parabolic wake pattern of the velocity (out-of-plane $x_\parallel - y_\perp$), which is what we measure, we need to differentiate Eq. (5) with respect to $\hat{t}$. Figure 3(a) shows the stationary phase approximation of the time derivative of Eq. (5) at $\hat{t} = 0$ and absolute $\hat{y}_\perp$ values. The two-dimensional interference pattern has ridges and zero values that conform to the shape of parabolas. All their focal points are located at the current position of the perturbation $(\hat{x}_\parallel, \hat{y}_\perp) = (0, 0)$. The focal lengths of the n confocal parabolas (i.e., the distance between their vertices and the current position of the perturbation), lying on the maximum ridges of the wake pattern, are given by $\widehat{f}_n = \phi_p + \pi/4 + 2\pi n$ in $(\hat{x}_\parallel, \hat{y}_\perp)$ coordinates. ϕ_p is a global constant phase shift depending on the details of the excitation physics and n is an integer labeling the considered parabola. For the out-of-plane velocity measured in our experiment, a phase ϕ_p equal to $\pi/2$ is expected and observed, since the maximum plate displacement of the wake field occurs at the point illuminated by the heating laser. These statements were cross-validated by numerical integral solutions and analytical stationary phase approximation as detailed in the Supplemental Material [35].

We now propose a geometrical construction of the parabolic pattern [Fig. 3(b)]. For this, one can draw parallel lines representing the wave fronts of specific narrow-band frequency components [similar to the examples from the measurement in Figs. 2(d)–2(i)]. These lines have inversely signed slopes [or angle φ in Figs. 2(d)–2(i)] for positive and negative $\hat{y}_\perp$, representing Mach cones with the symmetry line on the $x_\parallel$ axis. The relation between these slopes and the distance between two neighboring lines is defined by the dispersion relation (c_{ph} at specific frequency component), while the origin of the lines—intersection with the ordinate axis—is defined by ϕ_p. The lines are tangent to confocal parabolas with focal lengths $\widehat{f'}_n = \phi_p + 2\pi n$, as shown in the Supplemental Material [35]. This approach also allows us to recover the wake patterns associated with other dispersion relations, for example to compare with Kelvin wakes. When the line bundles are replaced by narrow-band frequency components (with the lines following the maxima of the two-dimensional sloped harmonic functions), a pattern similar to Fig. 3(a) emerges. The parabolas situated on the maximum ridge of this wake pattern are more open and have larger foci, shifted by $\pi/4$. This is because all the tangent lines fall outside the parabolas with focal lengths $\widehat{f'}_n = \phi_p + 2\pi n$.

The focal lengths of the confocal parabolas were measured experimentally by determining the position $x_\parallel$ of the maximum signal amplitude (and the first minimum signal amplitude in the positive direction from the maximum) for all the positions $y_\perp$, for all time instances when the parabolic wake pattern was within the scanned region, and for ten different v_p. The obtained mean values of the position $x_\parallel$ along with their standard deviation bands in rescaled coordinates $(\hat{x}_\parallel, \hat{y}_\perp)$ are presented in Fig. 3(c). The curves obtained at all ten different speeds (coded in gray shades) and at the increased α (blue) align with two confocal parabolas having focal lengths $3\pi/4$ (maximum) and $3\pi/4 + \pi$ (minimum). This provides validation for our mathematical models and the universality of the parabolic wake pattern.

Let us now derive the shape of the caustics depicted in Fig. 3(b). The waves are approximated as trains of lines defined by the condition $\vec{k} \cdot \vec{r} = 2\pi n$, where n is an integer,

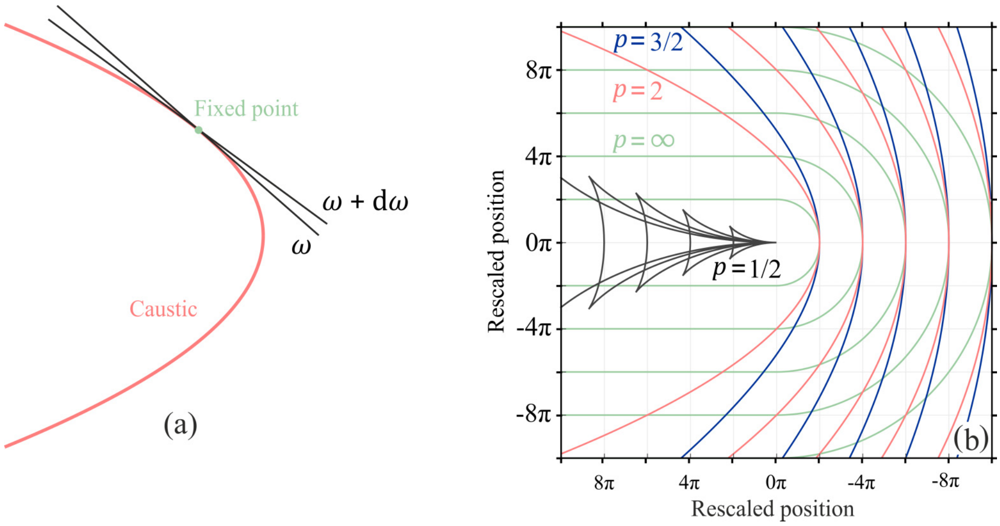

FIG. 4. Two wave fronts (black lines) that are close in frequency interfere constructively at a fixed point, depicted in green (a). We use this fixed-point condition to derive caustic wave patterns for arbitrary power laws (b), with the $p = 1/2$ (Kelvin wake, black), $p = 3/2$ (capillary wake, blue), $p = 2$ cases (parabolic wake, red), and $p = \infty$ (hypothetical, green).

$\vec{r} = (\hat{x}\ ,\hat{y}\ )$, and $\vec{k} = (\hat{k}_x, \hat{k}_y)$. Assuming a general power-law dispersion $\hat{\omega}(|\hat{k}|) = |\hat{k}|^p$ and using the direct equivalent of Eq. (3), this condition yields

$$\hat{x} = \frac{2\pi n}{\hat{\omega}} - \hat{y}\sqrt{\frac{\hat{\omega}^{\frac{2}{p}}}{\hat{\omega}^2} - 1}. \tag{6}$$

To find the caustic, we must find a point along this line that remains fixed under small variations in $\hat{\omega}$, as shown in Fig. 4(a). In particular, the $\hat{x}$ coordinate of this fixed point does not change under a small variation in $\hat{\omega}$, yielding the condition $\partial_{\hat{\omega}}\hat{x}\ = 0$. Together with Eq. (6), this allows us to solve for the coordinates of the caustic point associated to the angular frequency $\hat{\omega}$, namely

$$\begin{aligned}\hat{x} &= \frac{2\pi n}{p-1}\left(p\hat{\omega}^{1-\frac{2}{p}} - \hat{\omega}^{-1}\right),\\ \hat{y} &= p\frac{2\pi n}{p-1}\sqrt{\hat{\omega}^{-\frac{2}{p}} - \hat{\omega}^{2-\frac{4}{p}}}.\end{aligned} \tag{7}$$

This parametric expression contains the Kelvin-wake case ($p = 1/2$), the capillary-wave case ($p = 3/2$), and the case treated in the main text ($p = 2$). As shown in Fig. 4(b), it also allows us to recover the asymptotic pattern corresponding to p tending towards infinity. In our case of interest, $p = 2$, we can go further and remove $\hat{\omega}$ from Eq. (7). As expected, we obtain parabolic caustics satisfying

$$\hat{y}\ = 4\pi n\sqrt{1 - \frac{\hat{x}}{2\pi n}}. \tag{8}$$

To achieve the complete parabolic wake pattern, it is essential that the moving perturbation excites frequencies reaching at least until ω_{cr}. This condition is not fulfilled when the length of the perturbation spot L is excessively large or αv_p is overly high. In such cases, the parabolic wake pattern starts to open from the front, where the waves depart from the perturbation at $\varphi = 90^\circ$. Due to the lack of the frequency components with larger φ (having the wider cone opening), the parabolic wake pattern tends to approximate the shape of a Mach cone. This situation is similar to the transition between Kelvin and Mach regimes, wherein the cone openings are narrower than the Kelvin angle if low-frequency components are not excited, for instance in the case of excessively small objects moving on a water surface with too high velocity [6,7].

In analogy with the Mach number for nondispersive media and the Froude number for Kelvin wakes, a dimensionless number that governs these physics can be defined for media with quadratic dispersion, as $R = v_p\alpha L$. This number measures the ratio between the perturbation velocity and the critical velocity $v_{\mathrm{cr}} = 1/\alpha L$. The wake pattern has its complete shape around the vertices of parabolas when $R \leqslant 1$ [Figs. 1(b)–1(f)]. All frequency components up to ω_{cr} are excited if L is sufficiently small at specific v_p. This is not the case in Fig. 1(g). Since the laser is out of focus, the value of L is too high. At lower values of v_p, the criterion $R \leqslant 1$ is achieved for smaller L. In this case, the parabolas of the wake pattern will be closed at their vortices, however, they will have a smaller slope (longer focal lengths). In other words, only a limited area around the central part of the rescaled universal wake pattern will be visible.

To summarize, we provided an analytical explanation for experimentally observed parabolic wakes propagating in a medium with quadratic dispersion. We have shown that the observed pattern is universal once the coordinates are rescaled by the velocity and material factors. The equations define two regimes (propagating and evanescent) separated by ω_{cr}. In opposition to the Kelvin wake, the wave components below ω_{cr} produce the parabolic wake, while evanescent wave behavior is observable under the condition that the addressed frequency $\omega \geqslant \omega_{\mathrm{cr}}$. This condition is reminiscent to the critical angle behavior in the phenomenon of total reflection. The evanescent waves propagate solely along the trajectory of the moving perturbation, instead of along a spatial interface for the phenomenon of total reflection.

Our findings can be extended to other phenomena governed by quadratic (or even other power laws) dispersion, such as flexural phonons on graphene membranes [36–38] and specific regimes of polaritons in semiconductor microcavities [39–41].

We also demonstrated that Lamb waves can be generated not only by a laser pulse as a fast temporal change in illuminating power, but also by swift spatial movements of a continuous laser beam. This phenomenon holds potential for applications in contact-free damage detection and imaging of mechanical properties that influence the shape of the parabolic wake. Our findings may help to improve the understanding of elastic waves emitted by a moving crack front eventually occurring in silicon wafers [42–44].

In our experiment, the wave propagation properties were altered by inducing changes in the heat distribution at the spot of the moving perturbation. Interesting wave phenomena are anticipated to emerge as a consequence of interaction between the moving perturbation and the wake pattern that was excited at a prior temporal instance (similar to a study on water waves [45]). This situation occurs when the trajectory of the moving perturbation deviates from a straight path, when v_p is not constant, or when the intensity of the perturbation varies over time.

[1] W. Thomson, On ship waves, Proc. Inst. Mech. Eng. **38**, 409 (1887).

[2] F. S. Crawford, Elementary derivation of the wake pattern of a boat, Am. J. Phys. **52**, 782 (1984).

[3] L. James, Waves in fluids, Meas. Sci. Technol. **13**, 1501 (2002).

[4] J. W. Davys, R. J. Hosking, and A. D. Sneyd, Waves due to a steadily moving source on a floating ice plate, J. Fluid Mech. **158**, 269 (2006).

[5] T. Soomere, Nonlinear components of ship wake waves, Appl. Mech. Rev. **60**, 120 (2007).

[6] M. Rabaud and F. Moisy, Ship wakes: Kelvin or mach angle? Phys. Rev. Lett. **110**, 214503 (2013).

[7] A. Darmon, M. Benzaquen, and E. Raphaël, Kelvin wake pattern at large Froude numbers, J. Fluid Mech. **738**, R3 (2013).

[8] A. Likar and N. Razpet, Towards the Kelvin wake and beyond, Am. J. Phys. **81**, 245 (2013).

[9] J. Colen and E. B. Kolomeisky, Kelvin–Froude wake patterns of a traveling pressure disturbance, Eur. J. Mech. B: Fluids **85**, 400 (2021).

[10] F. Noblesse, J. He, Y. Zhu, L. Hong, C. Zhang, R. Zhu, and C. Yang, Why can ship wakes appear narrower than Kelvin's angle? Eur. J. Mech. B: Fluids **46**, 164 (2014).

[11] R. Pethiyagoda, T. J. Moroney, C. J. Lustri, and S. W. McCue, Kelvin wake pattern at small Froude numbers, J. Fluid Mech. **915**, A126 (2021).

[12] R. S. Johnson, *A Modern Introduction to the Mathematical Theory of Water Waves* (Cambridge University Press, Cambridge, UK, 1997).

[13] T. Von Kármán, *Aerodynamics* (McGraw-Hill, New York, 1963).

[14] R. H. Hernández and M. Sánchez, Localized Bénard-von Kármán vortex wake packets, Europhys. Lett. **58**, 222 (2002).

[15] M. Mokry, The vortex merger factor in aircraft wake turbulence, Aeronaut. J. **109**, 1 (2016).

[16] S. Wu, X. Zhai, and B. Liu, Aircraft wake vortex and turbulence measurement under near-ground effect using coherent Doppler lidar, Opt. Express **27**, 1142 (2019).

[17] A. M. Shevchenko and A. S. Shmakov, Experimental study of vortex wake behind of a wing at Mach number range of M = 2−4, AIP Conf. Proc. **2027**, 030103 (2018).

[18] J. H. Chen, B. J. Cantwell, and N. N. Mansour, The effect of Mach number on the stability of a plane supersonic wake, Phys. Fluids A **2**, 984 (1990).

[19] D. Winske, W. Daughton, D. S. Lemons, and M. S. Murillo, Ion kinetic effects on the wake potential behind a dust grain in a flowing plasma, Phys. Plasmas **7**, 2320 (2000).

[20] W. J. Miloch, Wake effects and Mach cones behind objects, Plasma Phys. Controlled Fusion **52**, 124004 (2010).

[21] E. B. Kolomeisky and J. P. Straley, Kelvin-mach wake in a two-dimensional fermi sea, Phys. Rev. Lett. **120**, 226801 (2018).

[22] J. B. Rosenzweig, D. B. Cline, B. Cole, H. Figueroa, W. Gai, R. Konecny, J. Norem, P. Schoessow, and J. Simpson, Experimental observation of plasma wake-field acceleration, Phys. Rev. Lett. **61**, 98 (1988).

[23] T. Katsouleas, Electrons hang ten on laser wake, Nature (London) **431**, 515 (2004).

[24] I. Blumenfeld, C. E. Clayton, F.-J. Decker, M. J. Hogan, C. Huang, R. Ischebeck, R. Iverson, C. Joshi, T. Katsouleas, N. Kirby, W. Lu, K. A. Marsh, W. B. Mori, P. Muggli, E. Oz, R. H. Siemann, D. Walz, and M. Zhou, Energy doubling of 42 GeV electrons in a metre-scale plasma wakefield accelerator, Nature (London) **445**, 741 (2007).

[25] M. Litos *et al.*, High-efficiency acceleration of an electron beam in a plasma wakefield accelerator, Nature (London) **515**, 92 (2014).

[26] A. Melzer, S. Nunomura, D. Samsonov, Z. W. Ma, and J. Goree, Laser-excited Mach cones in a dusty plasma crystal, Phys. Rev. E **62**, 4162 (2000).

[27] N. Razpet and A. Likar, Čerenkov radiation through the Hamiltonian approach, Am. J. Phys. **78**, 1384 (2010).

[28] P. Genevet, D. Wintz, A. Ambrosio, A. She, R. Blanchard, and F. Capasso, Controlled steering of Cherenkov surface plasmon wakes with a one-dimensional metamaterial, Nat. Nanotechnol. **10**, 804 (2015).

[29] A. J. Macleod, A. Noble, and D. A. Jaroszynski, Cherenkov radiation from the quantum vacuum, Phys. Rev. Lett. **122**, 161601 (2019).

[30] I. Carusotto, S. X. Hu, L. A. Collins, and A. Smerzi, Bogoliubov-Cerenkov radiation in a Bose-Einstein condensate flowing against an obstacle, Phys. Rev. Lett. **97**, 260403 (2006).

[31] F. Moisy and M. Rabaud, Mach-like capillary-gravity wakes, Phys. Rev. E **90**, 023009 (2014).

[32] J.-C. Ono-dit-Biot, M. Trejo, E. Loukiantcheko, M. Lauch, E. Raphaël, K. Dalnoki-Veress, and T. Salez, Hydroelastic wake on a thin elastic sheet floating on water, Phys. Rev. Fluids **4**, 014808 (2019).

[33] E. Raphaël and P. G. de Gennes, Capillary gravity waves caused by a moving disturbance: Wave resistance, Phys. Rev. E **53**, 3448 (1996).

[34] F. S. Crawford, Speed of gravity waves in deep water: Another elementary derivation, Am. J. Phys. **60**, 751 (1992).

[35] See Supplemental Material at http://link.aps.org/supplemental/10.1103/PhysRevResearch.6.L032027 for more details regarding the experiment and the refined analytical models.

[36] E. Mariani and F. von Oppen, Flexural phonons in free-standing graphene, Phys. Rev. Lett. **100**, 076801 (2008).

[37] W. L. Z. Zhao, K. S. Tikhonov, and A. M. Finkel'stein, Flexural phonons in supported graphene: From pinning to localization, Sci. Rep. **8**, 16256 (2018).

[38] A. Taheri, S. Pisana, and C. V. Singh, Importance of quadratic dispersion in acoustic flexural phonons for thermal transport of two-dimensional materials, Phys. Rev. B **103**, 235426 (2021).

[39] A. Amo, J. Lefrère, S. Pigeon, C. Adrados, C. Ciuti, I. Carusotto, R. Houdré, E. Giacobino, and A. Bramati, Superfluidity of polaritons in semiconductor microcavities, Nat. Phys. **5**, 805 (2009).

[40] C. Ciuti and I. Carusotto, Quantum fluid effects and parametric instabilities in microcavities, Phys. Status Solidi **242**, 2224 (2005).

[41] I. Carusotto and C. Ciuti, Probing microcavity polariton superfluidity through resonant rayleigh scattering, Phys. Rev. Lett. **93**, 166401 (2004).

[42] D. Landru, D. Massy, N. Ben Mohamed, O. Kononchuk, F. Mazen, S. Tardif, and F. Rieutord, Fracture wake patterns in brittle solids, Phys. Rev. Appl. **15**, 024068 (2021).

[43] D. Massy, F. Mazen, D. Landru, N. Ben Mohamed, S. Tardif, A. Reinhardt, F. Madeira, O. Kononchuk, and F. Rieutord, Crack front interaction with self-emitted acoustic waves, Phys. Rev. Lett. **121**, 195501 (2018).

[44] P. Ronseaux, F. Madeira, F. Mazen, D. Landru, O. Kononchuk, S. Tardif, and F. Rieutord, Experimental study of post-crack vibrations in dynamic fracture, J. Appl. Phys. **129**, 185103 (2021).

[45] C. d'Hardemare, S. Wildeman, A. Eddi, and E. Fort, Space-time folding of the wake produced by a supervelocity rotating point source, Phys. Rev. Lett. **122**, 104301 (2019).